

ACCEPTED MANUSCRIPT

System geometry optimization for molecular breast tomosynthesis with focusing multi-pinhole collimators

To cite this article before publication: Jarno van Roosmalen *et al* 2017 *Phys. Med. Biol.* in press <https://doi.org/10.1088/1361-6560/aa9265>

Manuscript version: Accepted Manuscript

Accepted Manuscript is "the version of the article accepted for publication including all changes made as a result of the peer review process, and which may also include the addition to the article by IOP Publishing of a header, an article ID, a cover sheet and/or an 'Accepted Manuscript' watermark, but excluding any other editing, typesetting or other changes made by IOP Publishing and/or its licensors"

This Accepted Manuscript is © 2017 Institute of Physics and Engineering in Medicine.

During the embargo period (the 12 month period from the publication of the Version of Record of this article), the Accepted Manuscript is fully protected by copyright and cannot be reused or reposted elsewhere.

As the Version of Record of this article is going to be / has been published on a subscription basis, this Accepted Manuscript is available for reuse under a CC BY-NC-ND 3.0 licence after the 12 month embargo period.

After the embargo period, everyone is permitted to use copy and redistribute this article for non-commercial purposes only, provided that they adhere to all the terms of the licence <https://creativecommons.org/licences/by-nc-nd/3.0>

Although reasonable endeavours have been taken to obtain all necessary permissions from third parties to include their copyrighted content within this article, their full citation and copyright line may not be present in this Accepted Manuscript version. Before using any content from this article, please refer to the Version of Record on IOPscience once published for full citation and copyright details, as permissions will likely be required. All third party content is fully copyright protected, unless specifically stated otherwise in the figure caption in the Version of Record.

View the [article online](#) for updates and enhancements.

1
2
3
4
5
6
7
8
9
10
11
12
13
14
15
16
17
18
19
20
21
22
23
24
25
26
27
28
29
30
31
32
33
34
35
36
37
38
39
40
41
42
43
44
45
46
47
48
49
50
51
52
53
54
55
56
57
58
59
60

System geometry optimization for Molecular Breast Tomosynthesis with focusing multi-pinhole collimators

Jarno van Roosmalen¹, Freek J Beekman^{1,2} and Marlies C Goorden¹

¹ Section Biomedical Imaging, Delft University of Technology, Delft, the Netherlands.

² MILabs B.V., Utrecht, the Netherlands

E-mail: j.vanroosmalen@tudelft.nl

Abstract Imaging of ^{99m}Tc labelled tracers is gaining popularity for detecting breast tumours. Recently, we proposed a novel design for molecular breast tomosynthesis (MBT) based on two sliding focusing multi-pinhole collimators that scan a modestly compressed breast. Simulation studies indicate that MBT has the potential to improve the tumour-to-background contrast-to-noise ratio significantly over state-of-the-art planar molecular breast imaging. The aim of the present paper is to optimize the collimator-detector geometry of MBT. Using analytical models, we first optimized sensitivity at different fixed system resolutions (ranging from 5 to 12 mm) by tuning the pinhole diameters and the distance between breast and detector for a whole series of automatically generated multi-pinhole designs. We evaluated both MBT with a conventional continuous crystal detector with 3.2 mm intrinsic resolution and with a pixelated detector with 1.6 mm pixels. Subsequently, full system simulations of a breast phantom containing several lesions were performed for the optimized geometry at each system resolution for both types of detector. From these simulations, we found that tumour-to-background contrast-to-noise ratio was highest for systems in the 7 mm to 10 mm system resolution range over which it hardly varied. No significant differences between the two detector types were found.

1. Introduction

The most common type of cancer affecting women is breast cancer; it constitutes 25 percent of all new female cancer cases worldwide and causes 15 % of all cancer related deaths in women (Ferlay *et al.*, 2015; Torre *et al.*, 2015). Breast cancer detection is being improved by advances in imaging technology. While X-ray mammography is still the most widely used modality, other breast imaging modalities that are being used include ultrasound, molecular breast imaging (MBI) with planar gamma cameras, magnetic resonance imaging, positron emission tomography, and digital breast tomosynthesis based on x-rays. An overview can be found in (Hruska and O'Connor, 2013) and (Fowler, 2014).

Recently, our group proposed a design for a novel Molecular Breast Tomosynthesis (MBT) scanner dedicated to imaging distributions of single-gamma emitting tracers in the breast (Beekman, 2014; van Roosmalen *et al.*, 2016). In the design, the patient lies prone on a bed with an opening for the breast, which is mildly compressed. Two scanning gamma cameras equipped with focusing multi-pinhole collimators acquire projections of the breast in a sequence of camera positions. The focusing collimator geometry combined with the possibility to confine the scan area enables to increase the signal from a suspected region of interest. A simulation study (van Roosmalen *et al.*, 2016) indicated that multi-pinhole MBT offers 3D localization of increased tracer uptake and may have the potential to increase tumour-to-background contrast-to-noise ratio (CNR) compared to planar MBI. As the pinhole geometry has a range of viewing angles of less than 180 degrees resulting in incomplete sampling, the term molecular tomosynthesis is used instead of SPECT. We introduced MBT in the earlier paper, but the system has not been optimized yet.

The first MBT design was based on conventional gamma detectors with a continuous NaI(Tl) scintillator read out by an array of photo-multiplier tubes (PMTs). Due to their cost effectiveness, these are still the most widely used detector types in SPECT and planar scintigraphy. However, there are more options (Peterson and Furenlid, 2011) as several new scintillation detectors are being investigated, e.g. those based on pixelated crystals, new light sensors and better detection algorithms. Moreover, semiconductor detectors like CZT, which can provide both high spatial and energy resolution, have become commercially available. As high-resolution detectors are typically much more expensive than conventional NaI(Tl) detectors, it is important to make a detector choice based on a thorough understanding of its ultimate impact on images.

As imaging characteristics depend on many properties such as sensitivity, system resolution, size of the field-of-view (FOV) and angular sampling over the FOV, it is not straightforward to design optimized multi-pinhole geometries. One of the complications is the way each of these properties depends on the many tuneable parameters. To fully consider their interdependence, optimization should be done on a complete system comprised of collimators and detectors, which can be done by performing

time-consuming full system simulations. However, this is not feasible for simulating a whole range of designs covering the entire parameter space. Therefore, we here take the approach of initially using analytical models to optimize sensitivity of MBT at a fixed system resolution. This optimization is repeated for a range of system resolutions (from 5 to 12 mm). After this analytical optimization, we evaluate optimized configurations with different system resolutions by complete system simulations of breast phantom images.

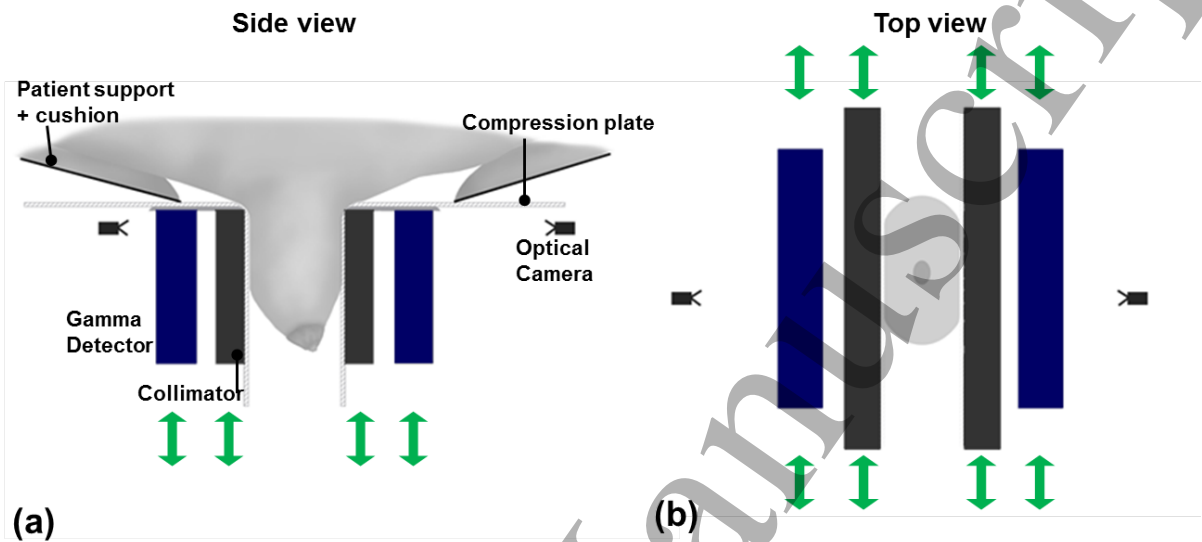


Figure 1 Schematic illustration of the geometry of the MBT scanner including compression plates, collimators, and gamma detectors. The green arrows indicate the directions into which the collimators and detectors can move. a) Side view showing breast of a woman lying prone on the scanner table. The breast is placed in the opening in the bed and slightly compressed. b) Top view of the breast between the transparent compression plates (artist impression).

2. Methods

In this section, we describe the basic design of MBT, the geometry optimization process and how we evaluate simulated images.

2.1 Molecular Breast Tomosynthesis

In the recently proposed MBT scanner (Beekman, 2014; van Roosmalen *et al.*, 2016), the patient lies prone on a specially designed bed, with the scanner underneath as detailed in figure 1. In our initial design, two Tungsten plates containing 63 pinholes each serve as collimators. They project the tracer distribution in the breast on conventional gamma detectors equipped with continuous 250 x 150 x 9.5 NaI(Tl) crystals (3.2 mm intrinsic resolution) placed 40 mm from the breast (parameter L in figure 2(a)). The pinholes in each of these collimator plates focus to a line at 40 mm distance from the collimator face ($F_x=40$ mm in figure 2(a)) and thus view a part of the breast. Such a focused design gives the MBT scanner the unique ability to focus on a user-defined volume-of-interest (VOI), which is beneficial because it can increase the count yield from the VOI (Beekman *et al.*, 2005; van der Have *et*

al., 2009). The VOI can be selected by the user on a graphical interface, which uses images taken by optical cameras that view the breast through the compression plates (Branderhorst *et al.*, 2011; Beekman, 2012). To image any volume, the FOV should be translated over the breast such that the desired scan volume is viewed over a range of angles (Vastenhouw and Beekman, 2007; Vaissier *et al.*, 2012). In MBT this is done by synchronized step-and-shoot movement of the collimators and detectors. For image reconstruction, all available information is taken into account, as the projection data from all positions is used simultaneously (Vastenhouw and Beekman, 2007).

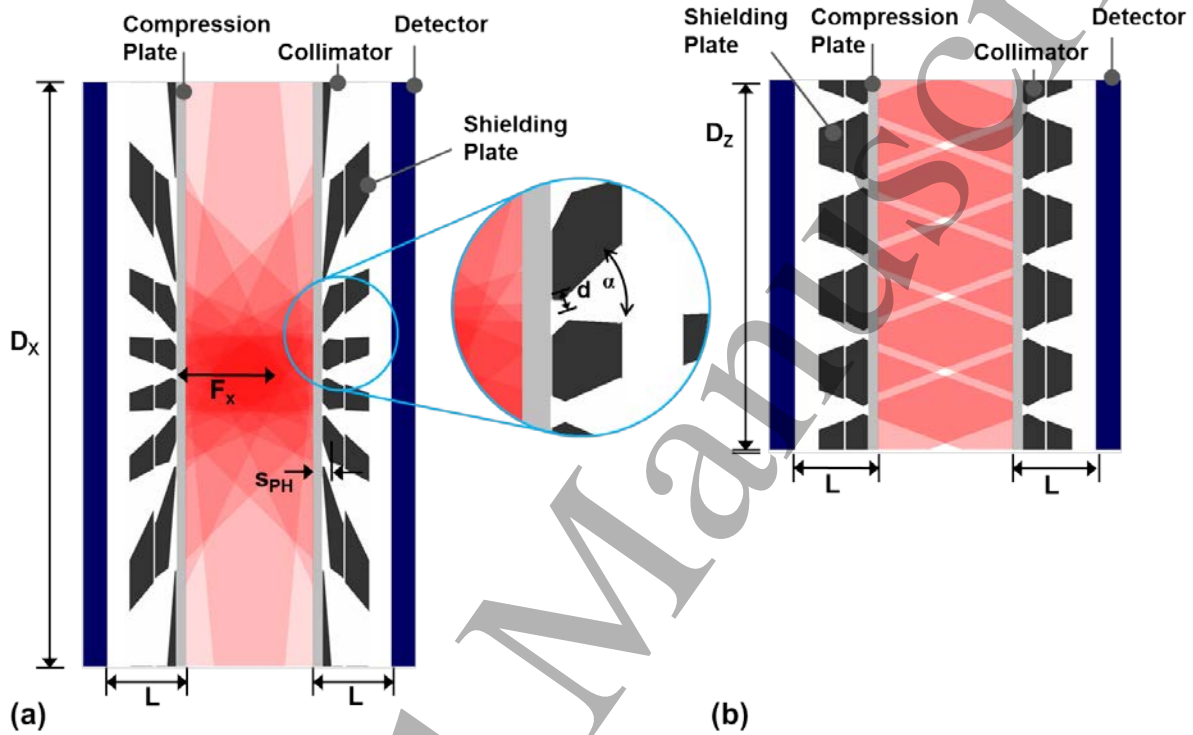


Figure 2 General design for MBT. The dark blue box represents the gamma detector, red shows the field-of-view, light grey the transparent compression plates, and dark grey the collimator and shielding plate. The different parameters are indicated in the figure. Two views are shown: (a) a coronal plane cross section and (b) a sagittal plane cross section.

2.2 System design

In this paper, we investigate the optimal collimator-detector set-up for MBT. In all designs, we assume that a lightly compressed breast is imaged with two focusing multi-pinhole collimators that each project onto a gamma detector. The collimator-detector geometry and the type of gamma detector are varied as explained below, and illustrated in figure 2(a&b).

Table 1 List of parameters for all geometries

Parameter	Description	Value	Varied/Fixed
L	Detector-breast distance		Free
D_x, D_z	Lateral dimensions of the detector	250, 150 mm	Fixed
R_i	Intrinsic spatial resolution of detector	1.6, 3.2 mm	consider 2 detectors
R_t	Targeted system resolution	5, 6, 7, 8, 9, 10, 11, 12 mm	We optimize sensitivity at several values
d	Pinhole diameter		Calculated to reach the targeted system resolution
α	Pinhole opening angle		Calculated to keep number of pinholes constant
s_{PH}	Distance between breast and pinhole centre	6 mm	Fixed at minimal feasible value

2.2.1 Considerations for collimator design. All parameters that together uniquely define a multi-pinhole collimator are listed in table 1. In principle, an infinite number of pinhole collimators can be considered when optimizing the designs, but we restrict ourselves by the following design principles.

- To account for the 4 mm thick compression plates and 2 mm between collimator surface and pinhole centre, a total distance is assumed between pinhole centre and breast of 6 mm.
- To prevent multiplexing related artefacts (Vunckx *et al.*, 2008; Mok *et al.*, 2009) we eliminate overlapping of projections by using a shielding plate in between collimator and detector (Beekman *et al.*, 2005; van Roosmalen *et al.*, 2016), see figure 2(a&b). Figure 3 shows how the opening angle γ and axis direction of the prismatoidic holes in the plate are linked to each of the pinholes. Each pinhole illuminates the entire rectangular hole in the shielding tube. The flood source projection in figure 4 shows that this results in tiled projections.
- We control the amount of focusing by fixing the distance from the collimator face to the line all pinhole axes point to (see figures 2(b) & 4) by setting the focal length $F_x=40$ mm (see figure 2(a)). This way all tested designs have a similarly sized FOV. We found that much stronger amounts of focusing were prohibited because in that case the outer pinholes were angulated so much that they started to overlap. On the other hand, if the focal length is too large, the benefits of focusing (described in section 2.1) are lost.
- The sizes of the pinhole projections on the detector depend on the choice of pinhole opening angle α (as pinhole opening angle and dimensions of holes in the shielding tube are directly linked, see point 2). Generally, increasing α will allow for less non-overlapping pinholes to be used but will also lead to a larger volume sensitivity per pinhole. Initial simulations showed that these effects cancel out meaning that the choice of opening angle does not have a large influence on the resolution-sensitivity trade-off. Thus, we decided to fix α for all pinholes in a

configuration, such that the central upper pinhole's projection (defined below) on the detector always has the same dimensions (25x25 mm).

Considering the design considerations described above, the pinhole diameter and the distance L between breast and detector are left as parameters to optimize the resolution-sensitivity trade-off.

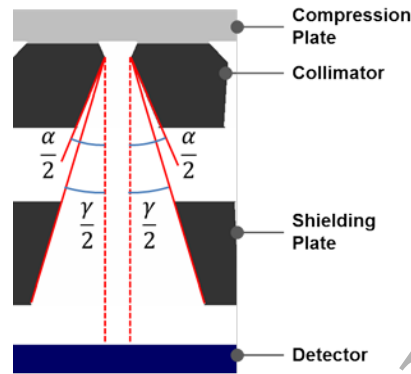


Figure 3 Schematic representation of cross section through a pinhole and the shielding plate. Indicated are the pinhole opening angle α and the opening angle for the hole in the shielding plate γ . Axis of pinhole and shielding plate hole are aligned.

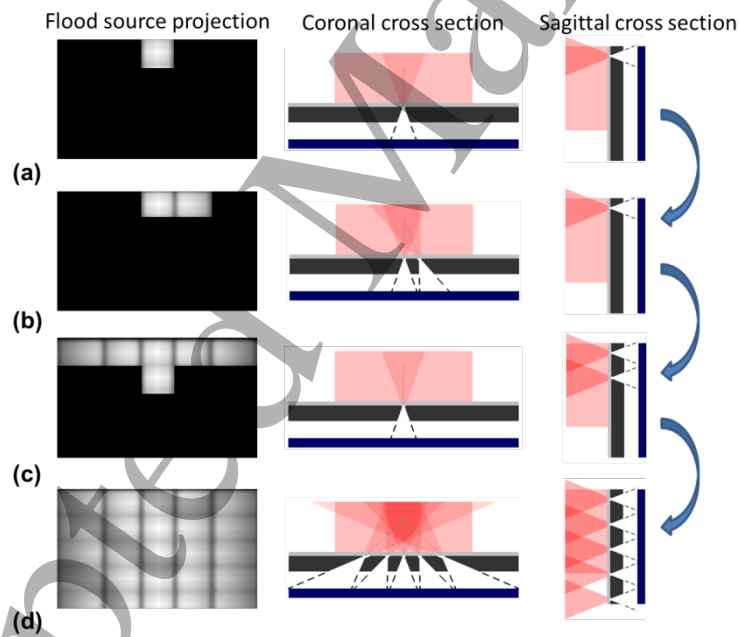


Figure 4 Schematic overview of the automatic pinhole placement. Flood source projection on the detector is shown as well as coronal and sagittal cross-section through collimator and detector. (a) The first pinhole is placed. (b) A subsequent pinhole is placed next to it the first pinhole such that projection is adjacent and non-overlapping (c) After filling one row, a pinhole is placed in the centre of the next row. (d) This process continues until the whole detector is filled with pinhole projections.

An important design aspect for a multi-pinhole collimator is the placement of the pinholes. The requirement to fill the detector with non-overlapping projections means that all pinholes must be re-positioned when e.g. L is varied. As we need to evaluate many configurations, we created an algorithm for automatic pinhole placement. The procedure used, as illustrated in figure 4, reads:

- a) Place a pinhole at the top centre of the collimator (i.e. closest to the breast and in the middle horizontally) such that its projection touches the edge of the detector (figure 4(a))
- b) Place the next pinhole to one side horizontally (using a line search) in such a position that the pinhole projections are separated by 3 mm (figure 4(b)).
- c) Repeat step b) on both sides until the border of the detector is reached. Then, start from the next row below (figure 4(c)).
- d) Repeat step b) and c) until the whole detector is filled (figure 4(d)).

2.2.2 Considerations for detector choice Detectors with continuous NaI(Tl) crystals read out by PMTs, as used in the initial MBT design, have the advantage of being cost effective and having a high detection efficiency (~90% for 140 keV photons). We assumed an intrinsic resolution of these detectors of 3.2 mm. In this paper, we will additionally evaluate the usefulness of high resolution pixelated detectors with 1.6 mm pixel size and a detection efficiency of ~70% for 140 keV photons. This corresponds to for example CZT detectors as applied in planar MBI (Hruska *et al.*, 2012) or pixelated NaI(Tl) crystals with PMT's. In the latter case the reflective material between the pixels reduces the efficiency (Rozler *et al.*, 2012). The two detectors types will henceforth be referred to as continuous and pixelated detector.

For breast imaging, it is important and challenging to also image breast tissue close to the chest wall. As in our earlier paper, we assume a dead edge of 5 mm for all detectors, which is achievable even with NaI(Tl) detectors read out by PMTs by using Maximum Likelihood processing (Milster *et al.*, 1990; Moore *et al.*, 2007; Barrett *et al.*, 2009). For all reported results, the appropriate detector efficiency for each detector type is taken into account, i.e. both in the analytical resolution-sensitivity calculations as in the full system simulations.

2.3 Analysis of different collimators and detectors based on sensitivity-resolution trade-off and simulation

In the analytical optimization study, the sensitivity is maximized at a fixed system resolution, as generally, when other characteristics are kept equal, more detected counts lead to an improved signal-to-noise ratio. We do this for a range of different target system resolutions from 5 to 12 mm. For each system resolution, the design with the highest sensitivity is selected for full system simulations.

We report sensitivity averaged over the breast shaped region described in section 2.5.1. In our design in which the detector and collimator are translated over a sequence of positions, sensitivity depends on the sequence chosen, which is provided in section 2.4. A sensitivity-weighted averaged resolution is determined over the same region, and the pinhole diameter is iteratively adjusted until the desired target system resolution is reached.

2.3.1 Resolution & Sensitivity formulas. We quickly estimate resolution and sensitivity by using the following formula (Metzler *et al.*, 2001) for the sensitivity g of a single knife-edge pinhole

$$g = \frac{d^2 \sin^3 \theta}{16h^2} + \frac{\sin^5 \theta \tan^2 \frac{\alpha}{2}}{8h^2 \mu^2} \left(1 - \frac{\cot^2 \theta}{\tan^2 \frac{\alpha}{2}} \right) \left(1 - \frac{\cot^2 \theta}{\tan^2 \frac{\alpha}{2}} + \mu d \csc \theta \cot \frac{\alpha}{2} \right). \quad (1)$$

Here θ is the angle between the plane perpendicular to the pinhole axis and the line from the pinhole centre to the source, μ the linear attenuation coefficient of the collimator (3.38 mm^{-1} for 140 keV photons in Tungsten) and h the perpendicular height of the source above the pinhole, other parameters were defined in table 1.

For system resolution, defined as the full width at half maximum (FWHM) of the point spread function, we use

$$R = \sqrt{d_e^2 \left(1 + \frac{1}{M} \right)^2 + \left(\frac{R_i}{M} \right)^2}, \quad (2)$$

where M is the magnification factor of the pinhole (i.e. the ratio between distance from source to pinhole, and pinhole to detector), d_e the effective pinhole diameter, and R_i the intrinsic detector resolution. Accorsi and Metzler (2004) derived effective diameters $d_{e\parallel}$ and $d_{e\perp}$ for the directions parallel and perpendicular to line of incidence on the detector, which are given by

$$d_{e\parallel} \approx d + \frac{\ln 2}{\mu} \left(\tan^2 \frac{\alpha}{2} - \cot^2 \theta \right) \cot \frac{\alpha}{2} \sin \theta, \quad (3)$$

$$d_{e\perp} \approx \sqrt{\left(d + \frac{\ln 2}{\mu} \tan \frac{\alpha}{2} \sin \theta \right)^2 - \left(\frac{\ln 2}{\mu} \right)^2 \cos^2 \theta}.$$

To arrive at one value for resolution we use the average of the two resolutions obtained by substituting the effective diameters in (2), as the effective resolution.

As mentioned above, we fix the size of the projection of the centre pinhole in the first row on the detector, by adjusting the opening angle to

$$\alpha = 2 \arctan \left(\frac{25 \text{ mm}/2}{L-6 \text{ mm}} \right). \quad (4)$$

For the continuous detector, a value of 3.2 mm is used for R_i , while a value of 1.6 mm is used for the pixelated detector. Note that in our analytical formulas we do not distinguish between continuous or pixelated crystals. As explained below, our full system simulations do take into account detector pixelation for the higher resolution detector.

2.4 Sampling & scan positions.

As mentioned above, the selected volume is imaged by moving the collimators in a sequence of steps. Movement takes place in the plane defined by the compression plates, i.e. either left-right (figure 1(b)), or up/down (figure 1(a)). In this paper, we use a sequence that covers the whole breast.

Ideally, one optimizes the scan sequence for a specific collimator. However, as we compare many designs and need to be sure we compare them equally, we use a single sequence with many closely spaced positions. This way we always get a uniform sensitivity regardless of the designs specific FOV pattern. For a single specific collimator one can design a scan sequence with a realistic number of positions, as we did in van Roosmalen *et al.* (2016).

The sequence we use consists of the collimators and detectors moving in the anterior direction in 2 mm steps for a total distance of 20 mm and from left to right in 8 mm steps from position -76 mm to 76 mm, where 0 mm denotes a collimator centred on the breast.

2.5 Validation by simulations of breast phantom scans

To validate the results from our analytical analysis and further analyse the most promising designs, we performed simulations for a few selected configurations. In these simulations, we accurately simulated gamma photon transport through our collimator, using a ray-tracing simulator (Wang *et al.*, 2017), which was used to both generate simulated projections and a system matrix for image reconstruction. This simulator uses the collimator modelled as a voxelized volume with a voxel size of 0.0625 mm as its input. The depth-of-interaction in the scintillator crystal is modelled by also raytracing the gamma photon through the scintillator, similarly as was described in (Goorden *et al.*, 2016). Consequently, the detector efficiency is automatically taken into account. For the continuous detector, we assumed 1.072 mm pixels in a 234x140 pixel grid and the intrinsic detector resolution was incorporated by modelling detector response with a 3.2 mm FWHM Gaussian. For the simulated pixelated detector systems, the detector was modelled using 1.6 mm pixels in a 156x94 pixel grid and no additional filter was applied.

To calculate phantom projections, we represented the phantoms on a regular grid with a source voxel size of 0.5 mm. The raytracer uses a threshold for ignoring small contributions which we set to 1% (Wang *et al.*, 2017). Moreover, the attenuation in the phantom was modelled using a uniform attenuation coefficient of 0.0151 mm^{-1} valid for 140 keV photons in water. We then generated phantom projections for each of the positions in the scan sequence accounting for the scanning time in each posi-

tion and added Poisson distributed noise to each projection. Earlier phantom studies for a similar geometry showed that scatter from the torso is not a significant problem for ^{99m}Tc -based tracers (Wang *et al.*, 1996; Hruska and O'Connor, 2006), which was confirmed in a simulation study for our MBT geometry (Wang *et al.*, 2017). Therefore, the use of a raytracer that models attenuation but ignores scatter is justified for this geometry.

For the tomographic reconstruction of the projection data, we used Maximum Likelihood Expectation Maximization (MLEM). The system matrix used in MLEM was determined at a 1.0 mm source voxel grid and a threshold of 2%. The discrepancy in grid size between phantom and reconstruction, and between cut off thresholds is to mimic a continuous activity distribution. Moreover, at this stage we decided not to apply an attenuation correction, as no method for accurately determining of the entire contour of the breast is yet established.

For the systems selected for full system simulations, the automatically generated designs were slightly tuned if needed to prevent pinholes at the edge to only have a small fraction of their projection on the detector, by adjusting the opening angle of all pinholes up to 5%. We checked that these small tunings resulted in changes in the analytically calculated resolution and sensitivities that were within 2.5 % of the unadjusted values.

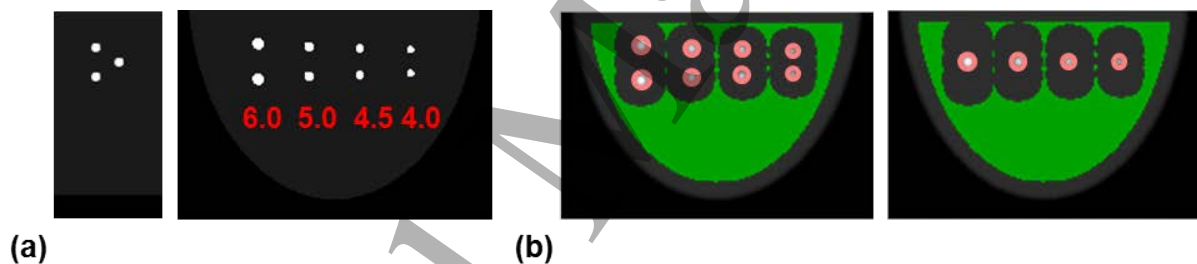


Figure 5 Slices through the breast phantom (a) left: slice parallel to sagittal plane through the 6.0 mm lesions, right: transverse slice at depth of two lesions. Lesion sizes indicated. (b). Transverse slices with red circles indicating the regions-of-interest used to determine the tumour signal while the green area denotes the background region.

2.5.1 Breast phantom In this paper, we use the same phantom as in our earlier work (van Roosmalen *et al.*, 2016). The breast is modelled as half an elliptically shaped disk (Dong *et al.*, 2011), with a 110 mm chest-to-nipple distance, a width of 150 mm, and a thickness of 55 mm. The phantom is placed such that the top of the activity is at the same place as the start of the useful field of view of the detector. To assess how differently sized lesions are imaged, we placed four sets with three lesions each in the phantom (6.0, 5.0, 4.5, 4.0 mm diameter), see figure 5(a). Within each set the central lesion was placed at a depth of 22 mm, with the other two lesions at a depth of 33 mm, making a triangular arrangement. We assumed a background activity concentration of 3.7 kBq/mL, consistent with an injection of 925 MBq ^{99m}Tc -Sestamibi (Hruska *et al.*, 2012; Mann *et al.*, 2012). We assume a concentration

of 37 kBq/ml in the lesions to give a tumour-background uptake ratio of 10:1 (Maublant *et al.*, 1996; Lee *et al.*, 2004; Hruska and O'Connor, 2008; Sullivan *et al.*, 2012). We set scan time of 10 minutes.

2.5.2 Analysis of images Besides visually inspecting different images, we compared different breast phantom images by calculating the tumour-to-background contrast-to-noise ratio (CNR) of the lesions given by

$$CNR = \frac{\bar{S} - \bar{B}}{\sigma_B}. \quad (5)$$

Here \bar{S} is the average signal taken in a spherical region placed on top of the lesion, \bar{B} is the average signal in a background region, and σ_B is the standard deviation in the background region and serves as measure of the noise. The regions used are indicated in figure 5(b). All simulations are repeated for 20 different noise realizations, and the average of the CNR values is reported.

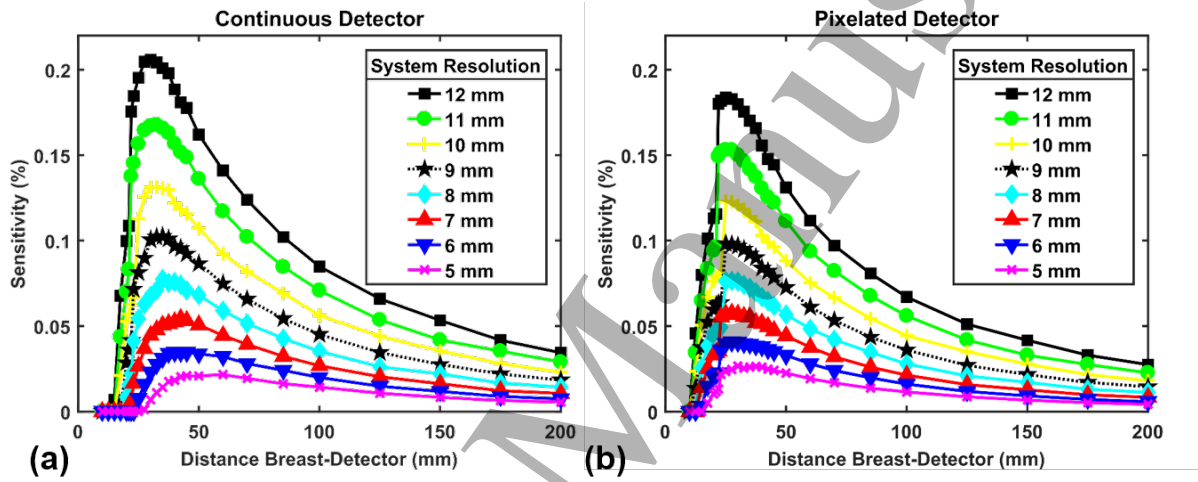


Figure 6 Volumetric sensitivity (averaged over the breast) as function of distance between detector and breast for (a) continuous detector, (b) pixelated detector. The lines indicate different fixed system resolutions R (5, 6, 7, 8, 9, 10, 11 and 12 mm).

3. Results

3.1 Analytical optimization

Results of the analytical optimization are shown in figure 6 in which sensitivity is shown as function of detector-breast distance for different fixed system resolutions (achieved by tuning the pinhole diameter). Note that every point in this graph represents the sensitivity of a different multi-pinhole geometry that was automatically generated by our script. Sensitivities for fixed system resolutions of 5 to 12 mm are shown for each detector. From the plots one can infer that, depending on the chosen system resolution, there is an optimal detector-breast distance at which sensitivity is maximal. The exact position of the optimum is determined by the relative contribution of two opposing effects. On one hand, placing the detector further away allows for larger pinhole magnification factors meaning that larger

pinhole diameters can achieve the same fixed system resolution, thus increasing the sensitivity. On the other hand, placing the detectors closer to the breast increases the solid angle at which detection can take place which also enhances sensitivity. The sensitivity drops rapidly at short detector-breast distances, as for these short distances the projections from the activity distribution on the detectors are not magnified anymore but minified and as a result the pinhole diameter is quickly shrinking to maintain resolution.

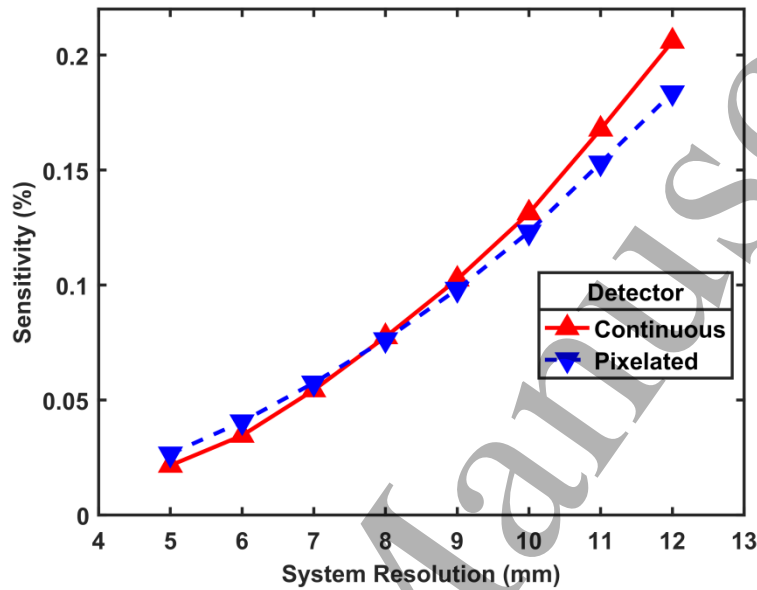


Figure 7 Plot of maximum reachable sensitivity as function of system resolution for both detector types. For each resolution, the detector-breast distance that gives the highest sensitivity at that fixed resolution is used (maximum in figure 6).

As expected, the curves in figure 6 indicate that the maximum sensitivity that can be obtained decreases as targeted system resolution improves. This dependence is shown in figure 7 for the two different detectors. The characteristics of the systems that obtain the maximum sensitivity at each system resolution are reported in tables 2 and 3. Although the higher resolution pixelated detector leads to collimators with higher sensitivities, this is offset by its lower detection efficiency. Overall a small improvement in sensitivity is reached with pixelated detectors if the targeted system resolution is 5 or 6 mm, while the continuous detector provides slightly higher sensitivity for the 9 to 12 mm target system resolutions.

3.2 Simulation results

Full system simulations were performed for each of the optimal configurations (maximum in figure 6, and geometries summarized in tables 2 and 3). We checked that sensitivities extracted from system matrices that were generated in these simulations were close to those predicted by the analytical expressions (<4% difference) which partly validates our analytical analysis.

1
2
3
4
5
6
7
8
9
10
11
12
13
14
15
16
17
18
19
20
21
22
23
24
25
26
27
28
29
30
31
32
33
34
35
36
37
38
39
40
41
42
43
44
45
46
47
48
49
50
51
52
53
54
55
56
57
58
59
60

The appearance of breast phantom images resulting from these simulations depends on the number of iterations used and the FWHM of the Gaussian filter applied. The optimal combination of these parameters can strongly depend on system resolution and sensitivity. For a fair comparison, we determined an optimal combination of iteration number and filter level in the following way: Gaussian filters with FWHM ranging from 0 to 8 mm (in 1 mm steps) were applied to all images and the iteration number and filter combination that lead to the highest CNR in the 6.0 mm lesions (on average over the noise realizations) was determined, requiring at least 5 iterations to ensure a minimum level of convergence. This optimal number of iterations and filter and the achieved optimal CNR for 6.0 mm lesions are also provided in tables 2 and 3.

Table 2 Details of simulated systems with 3.2 mm intrinsic resolution continuous detector. Parameters of geometries that maximize sensitivity (and are thus simulated) are provided for each system resolution. The iteration number and filter size to reach the maximal CNR for the 6.0 mm lesion in reconstructed images are provided.

System Resolution (mm)	5.0	6.0	7.0	8.0	9.0	10.0	11.0	12.0
Detector-breast distance (mm)	47.5	40	40	35	35	32.5	32.5	30
Pinhole diameter (mm)	1.98	2.21	2.75	3.01	3.49	3.72	4.13	4.27
Pinhole opening angle (degree)	29	35	35	39	39	42	42	45
Volumetric Sensitivity over whole breast (%)	0.022	0.035	0.054	0.077	0.102	0.131	0.168	0.206
Sensitivity in focus (%)	0.087	0.129	0.191	0.259	0.346	0.424	0.520	0.601
Optimal Iteration	11	14	16	17	17	19	20	21
Optimal filter FWHM (mm)	5	4	4	3	2	1	1	0
Optimal CNR	8.5	9.8	10.5	10.6	10.3	10.6	9.9	9.1

Table 3 Details of simulated systems with 1.6 mm pixelated detector. Parameters of geometries that maximize sensitivity (and are thus simulated) are provided for each system resolution. The iteration number and filter size to reach the maximal CNR for the 6.0 mm lesion in reconstructed images are provided.

System Resolution (mm)	5.0	6.0	7.0	8.0	9.0	10.0	11.0	12.0
Detector-breast distance (mm)	30	27.5	27.5	27.5	25	25	25	25
Pinhole diameter (mm)	1.67	1.92	2.32	2.71	2.84	3.21	3.56	3.91
Pinhole opening angle (degree)	45	49	49	49	53	53	53	53
Volumetric Sensitivity over whole breast (%)	0.027	0.041	0.057	0.076	0.098	0.123	0.153	0.184
Sensitivity in focus (%)	0.083	0.119	0.171	0.227	0.273	0.341	0.487	0.487
Optimal Iteration	12	14	15	16	17	17	19	19
Optimal filter FWHM (mm)	4	4	4	3	3	2	2	2
Optimal CNR	9.2	9.4	10.4	10.4	10.5	10.0	9.8	9.2

Figure 8 shows images at three filter levels with the most optimal filter level marked with a red boundary. Each image is shown with the optimal number of iterations for that filter level. From these images, it is difficult to distil any clear differences in performance for the different systems. In the higher resolution systems, the spheres are slightly less elongated between the two collimator plates, but the background also contains more noise, especially close to the collimator. The shown images for each system are for the noise realisation with CNR closest to the median for that system. Profiles through the 6.0 mm lesions are shown in Figure 9 for a fixed 3 mm filter and the 50th percentile noise realization, i.e. the image shown in figure 8. When the targeted system resolution is worse, contrast recovery is lower as can be expected. Figure 10 shows the optimum CNR for each simulated system. We infer from figure 10 that for the 6.0 mm lesion, the highest CNR is achieved by the 7 mm to 10 mm system resolution systems. Moreover, we see for none of the lesions sizes any clear difference between the continuous and pixelated detector systems. Note that 5.0 mm lesions have CNR values close to the detection limit (CNR of 4-5 as given by the Rose- criterion (Currie, 1968; Rose, 1973; Cherry *et al.*, 2012)), while the smallest lesions score clearly below the limit for all systems.

1
2
3
4
5
6
7
8
9
10
11
12
13
14
15
16
17
18
19
20
21
22
23
24
25
26
27
28
29
30
31
32
33
34
35
36
37
38
39
40
41
42
43
44
45
46
47

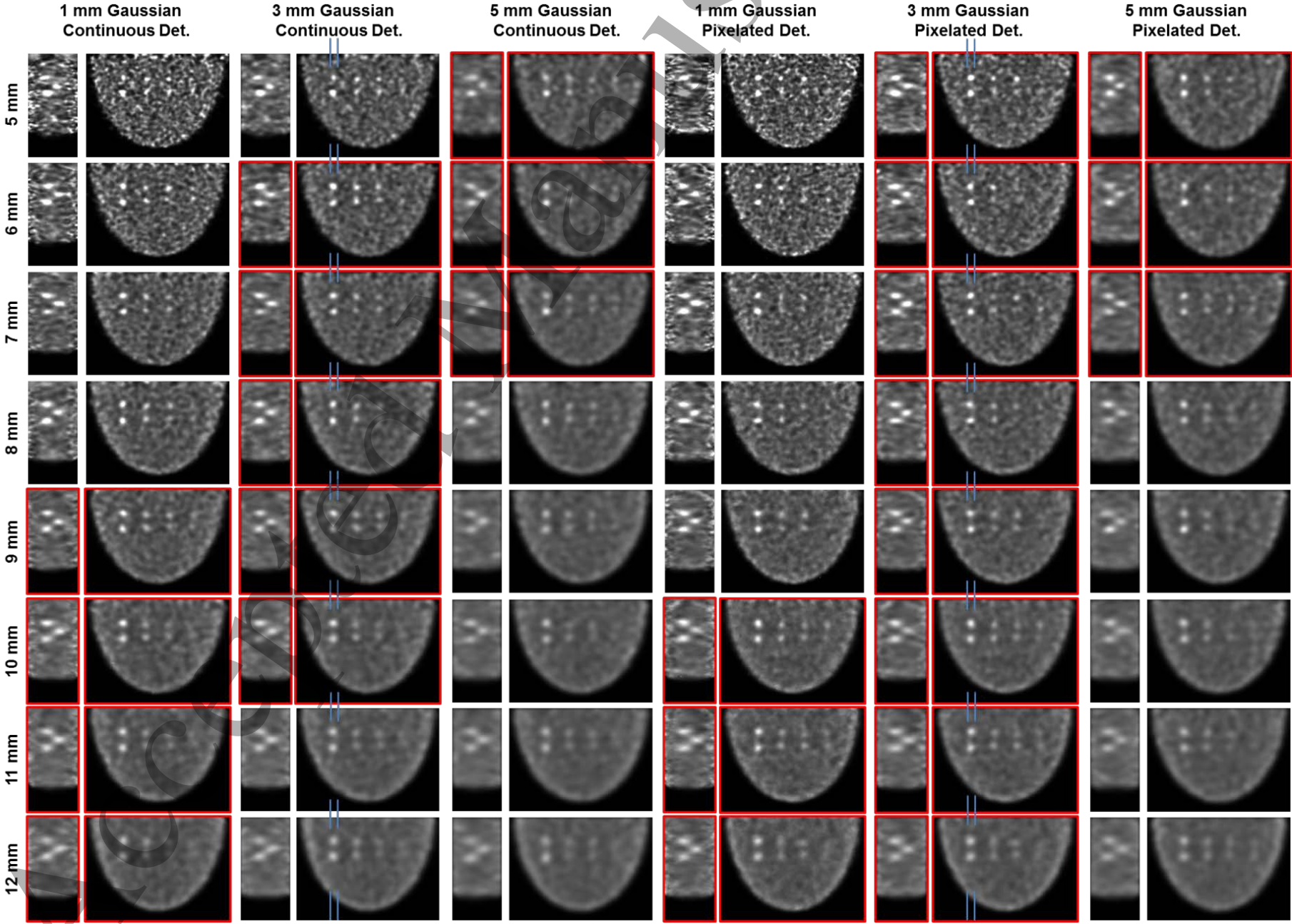


Figure 8 Simulated images of a breast shaped phantom containing lesions of 4.0, 4.5, 5.0 and 6.0 mm. Alternating images show sagittal slices through the lesions, and transverse slices at the depth of two lesions. Each row represents a different target system resolution, while different columns show different filter levels (1.0, 3.0 and 5.0 mm FWHM Gaussian filter) and different detector types (Continuous or Pixelated). The number of iterations for each image is as listed in tables 2 and 3. The red boxes in each row indicate the filter levels that result in the highest CNR for the 6.0 mm lesions for that system. Blue lines indicate location of profiles shown in figure 10.

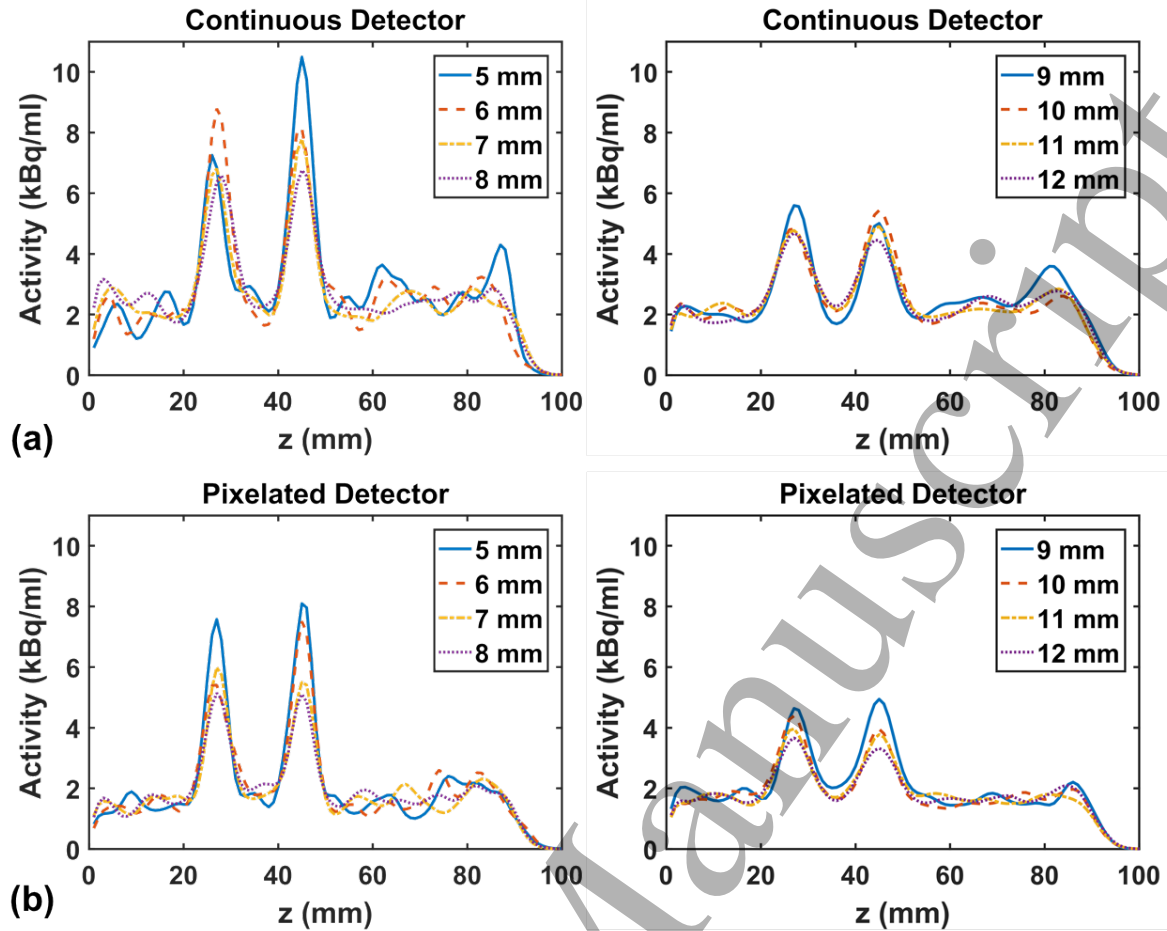


Figure 9 Profiles through the 6.0 mm lesions, with position as indicated in figure 8, for 3.0 mm FWHM Gaussian filter. Different lines indicate different targeted system resolutions. (a) Profiles obtained with 3.2 mm intrinsic resolution continuous NaI(Tl) detector, (b) for 1.6 mm pixelated CZT detector.

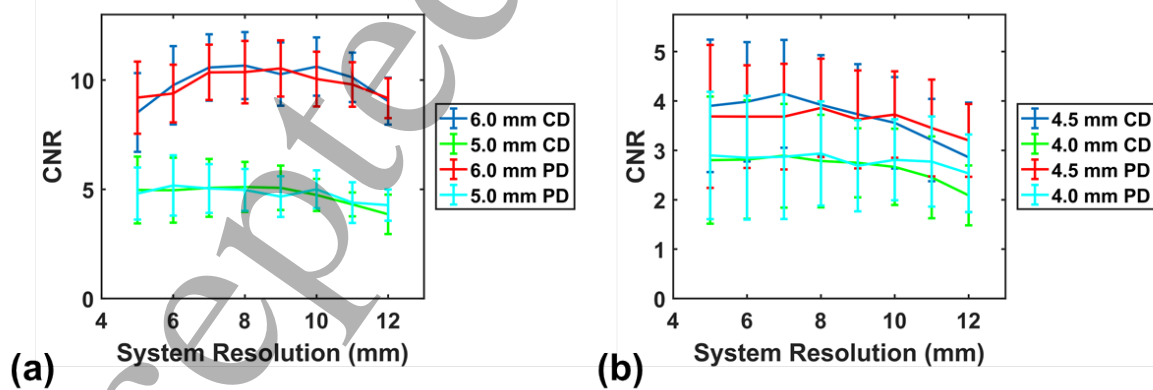


Figure 10 Plot of best CNR for each system resolution for (a) the 6.0 and 5.0 mm lesions and (b) the 4.5 and 4.0 mm lesions. Maximum taken over iterations 5 to 32 and filters from 0 to 10 mm FWHM, as indicated in table 2 and 3. The different lines represent the different lesion sizes and detector types (Continuous Detector (CD) and Pixelated Detector (PD)) and the error bars are the standard deviation in CNR for the 20 noise realisations.

4. Discussion

In this paper, we optimized focusing multi-pinhole configurations to find the geometry that achieves the highest spatial resolution-sensitivity trade-off.

Ideally, one would like to choose the system that is best suited for the imaging task at hand, which in this case is tumour detection. To determine detectability a numerical observer like the channelized Hotelling observer that mimics human observers is often used. However, a proper evaluation requires a huge number of noise realizations per system, making such a comparison computationally very expensive. A preliminary test indicated several hundreds of noise realizations per system would be required for MBT. We estimate that using 40 processor cores, this would take at least several years of simulations, which is prohibitively long for the scope of the current research project.

The tumour-to-background contrast-to-noise (CNR) ratio that we used is also linked to detectability via the Rose-criterion (Currie, 1968; Rose, 1973; Cherry *et al.*, 2012) and a relevant indicator for the possibility to use quantification to find heightened uptake regions. Moreover, CNR does not require many noise realizations and can quickly be calculated for many systems, iterations and filter levels. Therefore, we compare the CNR for optimized geometries with different fixed system resolutions.

In this paper, we only maximised sensitivity for a whole breast imaging sequence. In our earlier work, we showed that focusing on a lesion can significantly improve the CNR. Ideally one would like to focus on each lesion in the optimization study. However, this would require 4 times more simulations than for the whole breast optimization. The computational time required for all the simulations for this paper was already very high (i.e. almost 2 months on several multi-CPU systems totalling 80 cores), so more simulations were deemed infeasible for now. We do report the sensitivity that can be achieved in focusing mode in tables 2 and 3. These sensitivities are as reached by the optimal system for whole breast imaging.

The design used in our earlier work (van Roosmalen *et al.*, 2016), was not optimized. The initial design was based on a system resolution of 5.8 mm and had a sensitivity of 0.033%, which is very similar to the 6.0 mm system resolution system from this paper. We here see that by trading a bit of resolution for sensitivity a higher CNR can be reached.

Overall, the different systems for the system resolutions of 7 to 10 mm show minor differences in performance in terms of CNR. One notes that for 7 mm system resolution optimal CNR is obtained with a filter of 4 mm FWHM, and for 10 mm system resolution a filter of 1 mm or 2 mm is preferable for the continuous and pixelated detectors respectively. So, it seems that one can choose between higher resolution systems with more post-filtering or lower resolution system with a smaller post filter, within this

range. The two detector types give very similar results, but as continuous detectors are much cost effective, the continuous NaI(Tl) based detector seems to be the best choice.

We think that in future work it may be worth to compare other focusing collimators such as fan beam or slit-slat collimators (Daekwang and Metzler, 2012) with the focusing pinhole geometries considered in this work.

5. Conclusion

We found that the optimal pinhole collimator for molecular breast tomosynthesis for the detection of 6.0 mm lesions uses a system resolution in the 7 to 10 mm range. Use of either a 3.2 mm intrinsic resolution continuous detector or a 1.6 mm pixels pixelated detector did barely influence the results.

Acknowledgements

This work is supported by the Dutch Organization for Scientific Research (NWO) under the VIDI grant 12371 'Focused imaging of tumors'.

References

- Accorsi R and Metzler S D 2004 Analytic determination of the resolution-equivalent effective diameter of a pinhole collimator *IEEE Trans Med Imaging* **23** 750-63
- Barrett H H, Hunter W C J, Miller B W, Moore S K, Yichun C and Furenlid L R 2009 Maximum-Likelihood Methods for Processing Signals From Gamma-Ray Detectors *IEEE Trans. Nucl. Sci* **56** 725-35
- Beekman F J 2012 Radiation detection device, scintillation device and detection method, as well as multiple image-forming device (Patent: US 12/083,383).
- Beekman F J 2014 Gamma radiation breast imaging apparatus (Patent: US 14/044,019, NL 2009566).
- Beekman F J, van der Have F, Vastenhouw B, van der Linden A J, van Rijk P P, Burbach J P and Smidt M P 2005 U-SPECT-I: a novel system for submillimeter-resolution tomography with radiolabeled molecules in mice *J. Nucl. Med.* **46** 1194-200
- Branderhorst W, Vastenhouw B, van der Have F, Blezer E A, Bleeker W and Beekman F 2011 Targeted multi-pinhole SPECT *Eur. J. Nucl. Med. Mol. Imag.* **38** 552-61
- Cherry S R, Sorenson J A and Phelps M E 2012 *Physics in nuclear medicine*: Elsevier Health Sciences)
- Currie L A 1968 Limits for qualitative detection and quantitative determination. Application to radiochemistry *Analytical Chemistry* **40** 586-93
- Daekwang K and Metzler S D 2012 Finding Optimized Conditions of Slit-Slat and Multislit-Slat Collimation for Breast Imaging *Nuclear Science, IEEE Transactions on* **59** 62-9
- Dong S-L, Chu T-C, Lan G-Y, Lin Y-C, Yeh Y-H and Chuang K-S 2011 Development of an Adjustable Model Breast for Mammographic Dosimetry Assessment in Taiwanese Women *Am. J. of Roentgenology* **196** W476-W81
- Ferlay J, Soerjomataram I, Dikshit R, Eser S, Mathers C, Rebelo M, Parkin D M, Forman D and Bray F 2015 Cancer incidence and mortality worldwide: Sources, methods and major patterns in GLOBOCAN 2012 *International Journal of Cancer* **136** E359-E86
- Fowler A M 2014 A Molecular Approach to Breast Imaging *J. Nucl. Med.* **55** 177-80
- Goorden M C, van Roosmalen J, van der Have F and Beekman F J 2016 Optimizing modelling in iterative image reconstruction for preclinical pinhole PET *Phys. Med. Biol.* **61** 3712-33
- Hruska C B and O'Connor M K 2006 CZT detectors: How important is energy resolution for nuclear breast imaging? *Physica Medica* **21** 72-5
- Hruska C B and O'Connor M K 2008 Quantification of lesion size, depth, and uptake using a dual-head molecular breast imaging system *Med. Phys.* **35** 1365-76
- Hruska C B and O'Connor M K 2013 Nuclear imaging of the breast: Translating achievements in instrumentation into clinical use *Med. Phys.* **40** 050901
- Hruska C B, Weinmann A L and O'Connor M K 2012 Proof of concept for low-dose molecular breast imaging with a dual-head CZT gamma camera. Part I. Evaluation in phantoms *Med. Phys.* **39** 3466-75
- Lee T, Braun K, Jaszczak R, Bowsher J and Bobkov K *Nucl. Sci. Symp. Conf. Rec.* (2004), vol. Series) pp 3352-6 Vol. 5

- 1
- 2
- 3 Mann S D, Perez K L, McCracken E K, Shah J P, Wong T Z and Tornai M P 2012 Initial In Vivo Quantification of Tc-99m
- 4 Sestamibi Uptake as a Function of Tissue Type in Healthy Breasts Using Dedicated Breast SPECT-CT *J. Onco.* **2012**
- 5 Maublant J, de Latour M, Mestas D, Clemenson A, Charrier S, Feillel V, Le Bouedec G, Kaufmann P, Dauplat J and Veyre A
- 6 1996 Technetium-99m-sestamibi uptake in breast tumor and associated lymph nodes *J. Nucl. Med.* **37** 922-5
- 7 Metzler S D, Bowsher J E, Smith M F and Jaszczak R J 2001 Analytic determination of pinhole collimator sensitivity with
- 8 penetration *IEEE Trans Med Imaging* **20** 730-41
- 9 Milster T D, Aarsvold J N, Barrett H H, Landesman A L, Mar L S, Patton D D, Roney T J, Rowe R K and Seacat R H 1990 A Full-
- 10 Field Modular Gamma Camera *J. Nucl. Med.* **31** 632-9
- 11 Mok G S P, Yuchuan W and Tsui B M W 2009 Quantification of the Multiplexing Effects in Multi-Pinhole Small Animal SPECT:
- 12 A Simulation Study *IEEE Trans. Nucl. Sci* **56** 2636-43
- 13 Moore S K, Hunter W C J, Furenlid L R and Barrett H H *Nucl. Sci. Symp. Conf. Rec, 2007*, vol. Series) pp 3691-4 Vol. 5
- 14 Peterson T E and Furenlid L R 2011 SPECT detectors: the Anger Camera and beyond *Phys. Med. Biol.* **56** R145
- 15 Rose A 1973 *Vision: human and electronic*: Plenum Press, New York)
- 16 Rozler M, Liang H, Sabet H and Chang W 2012 Development of a cost-effective modular pixelated NaI(Tl) detector for
- 17 clinical SPECT applications *IEEE Trans. Nucl. Sci* **59** 1831-40
- 18 Sullivan O, Gong Z, Klanian K, Patel T and Williams M 2012 *Breast Imaging*, ed A A Maidment, et al.: Springer Berlin
- 19 Heidelberg) pp 300-7
- 20 Torre L A, Bray F, Siegel R L, Ferlay J, Lortet-Tieulent J and Jemal A 2015 Global cancer statistics, 2012 *CA: A Cancer Journal*
- 21 *for Clinicians* **65** 87-108
- 22 Vaissier P E B, Goorden M C, Vastenhouw B, van der Have F, Ramakers R M and Beekman F J 2012 Fast Spiral SPECT with
- 23 Stationary γ -Cameras and Focusing Pinholes *J. Nucl. Med.* **53** 1292-9
- 24 van der Have F, Vastenhouw B, Ramakers R M, Branderhorst W, Krah J O, Ji C, Staelens S G and Beekman F J 2009 U-SPECT-
- 25 II: An Ultra-High-Resolution Device for Molecular Small-Animal Imaging *J. Nucl. Med.* **50** 599-605
- 26 van Roosmalen J, Goorden M C and Beekman F J 2016 Molecular breast tomosynthesis with scanning focus multi-pinhole
- 27 cameras *Phys. Med. Biol.* **61** 5508-28
- 28 Vastenhouw B and Beekman F 2007 Submillimeter total-body murine imaging with U-SPECT-I *J. Nucl. Med.* **48** 487-93
- 29 Vunckx K, Suetens P and Nuyts J 2008 Effect of Overlapping Projections on Reconstruction Image Quality in Multipinhole
- 30 SPECT *IEEE Trans. Med. Imag.* **27** 972-83
- 31 Wang B, Roosmalen J v, Piët L, van Schie M A, Beekman F J and Goorden M C 2017 Voxelized ray-tracing simulation
- 32 dedicated to multi-pinhole molecular breast tomosynthesis *Biomed. Phys. Eng. Express* **3** 045021
- 33 Wang H, Scarfone C, Greer K L, Coleman R E and Jaszczak R J *Nucl. Sci. Symp. Conf. Rec, 1996*, vol. Series 2) pp 1387-91 vol.2
- 34
- 35
- 36
- 37
- 38
- 39
- 40
- 41
- 42
- 43
- 44
- 45
- 46
- 47
- 48
- 49
- 50
- 51
- 52
- 53
- 54
- 55
- 56
- 57
- 58
- 59
- 60